Weierstraß-Institut
für Angewandte Analysis und Stochastik
Leibniz-Institut im Forschungsverbund Berlin e. V.

Preprint ISSN 2198-5855

Fast scatterometric measurement of periodic surface structures in plasma-etching processes

Wolfgang Matthias Klesse[1], Andreas Rathsfeld[2],

Claudine Groß[3], Enno Malguth[1], Oliver Skibitzki[2], Lahbib Zealouk[3]

submitted: December 21, 2018

[1] IHP-Leibniz-Institut für innovative Mikroelektronik
im Technologiepark 25
12536 Frankfurt (Oder)
Germany
E-Mail: klesse@ihp-microelectronics.com
skibitzki@ihp-microelectronics.com

[2] Weierstrass Institute
Mohrenstr. 39
10117 Berlin
Germany
E-Mail: andreas.rathsfeld@wias-berlin.de

[3] LayTec AG
Seesener Str. 10-13
10709 Berlin
Germany
E-Mail: claudine.gross@laytec.de
enno.malguth@laytec.de

No. 2564
Berlin 2018

2010 *Mathematics Subject Classification.* 65N21, 35Q61.

2008 *Physics and Astronomy Classification Scheme.* 42.40.Lx.

Key words and phrases. Scatterometry, inverse problem, time-harmonic Maxwell's equation.

The work on this paper has been supported by the program "Zentrales Innovationsprogramm Mittelstand" of the Federal Ministry for Economic Affairs and Energy (KF 2279503AB4).

Edited by
Weierstraß-Institut für Angewandte Analysis und Stochastik (WIAS)
Leibniz-Institut im Forschungsverbund Berlin e. V.
Mohrenstraße 39
10117 Berlin
Germany

Fax: +49 30 20372-303
E-Mail: preprint@wias-berlin.de
World Wide Web: http://www.wias-berlin.de/

Fast scatterometric measurement of periodic surface structures in plasma-etching processes

Wolfgang Matthias Klesse, Andreas Rathsfeld,
Claudine Groß, Enno Malguth, Oliver Skibitzki, Lahbib Zealouk

Abstract

To satisfy the continuous demand of ever smaller feature sizes, plasma etching technologies in microelectronics processing enable the fabrication of device structures with dimensions in the nanometer range. In a typical plasma etching system a plasma phase of a selected etching gas is activated, thereby generating highly energetic and reactive gas species which ultimately etch the substrate surface. Such dry etching processes are highly complex and require careful adjustment of many process parameters to meet the high technology requirements on the structure geometry.

In this context, real-time access of the structure's dimensions during the actual plasma process would be of great benefit by providing full dimension control and film integrity in real-time. In this paper, we evaluate the feasibility of reconstructing the etched dimensions with nanometer precision from reflectivity spectra of the etched surface, which are measured in real-time throughout the entire etch process. We develop and test a novel and fast reconstruction algorithm, using experimental reflection spectra taken about every second during the etch process of a periodic 2D model structure etched into a silicon substrate.

Unfortunately, the numerical simulation of the reflectivity by Maxwell solvers is time consuming since it requires separate time-harmonic computations for each wavelength of the spectrum. To reduce the computing time, we propose that a library of spectra should be generated before the etching process. Each spectrum should correspond to a vector of geometry parameters s.t. the vector components scan the possible range of parameter values for the geometrical dimensions. We demonstrate that by replacing the numerically simulated spectra in the reconstruction algorithm by spectra interpolated from the library, it is possible to compute the geometry parameters in times less than a second. Finally, to also reduce memory size and computing time for the library, we reduce the scanning of the parameter values to a sparse grid.

1 Introduction

Surface structures with dimensions in the nanometer range are employed in numerous applications, such as diffractive optical elements, micro-electromechanical system, semiconductors, and lasers. To transfer the desired pattern defined by lithography into the substrate surface reactive-ion-etching (RIE) plays a key role. The main principle of this dry plasma etching technology is to harness the interactions between the substrate and highly reactive radicals of weakly ionized plasmas operating in non-equilibrium. Removal of the top layers of the substrate surface within the plasma is achieved by either ion sputtering processes or chemical reactions of dissociated etchant gas species, which readily turn surface atoms into a volatile gas. In contrast to wet chemical etching techniques, the combination of high energy ion bombardment and highly reactive radicals allows for precise engineering of RIE processes in terms of optimal anisotropic etching, selectivity against the etch mask, and fast etch rates. However, any plasma etching approach involves various complex plasma and pattern-related

DOI 10.20347/WIAS.PREPRINT.2564 Berlin 2018

phenomena which are not fully understood and challenging to control (cf. [34]). Already minimal fluctuations and instabilities of the etching parameters (i.e. RF power, gas flow rate, chamber pressure etc.) may lead to significant variations of the targeted profile of two- and three-dimensional etch patterns.

Therefore, full control of the etch process requires real-time monitoring of the time-dependent geometrical structure dimensions. For example, in the case of a simple model system of two-dimensional periodic line-space structures with trapezoidal multi-layer terraces, all critical geometrical parameters, like widths, heights, side-wall angles, and radii of corner rounding, should be accessible throughout the etch process to guarantee satisfactory etch results within the tolerance limits. Comparing the reflectance spectra of the developing surface structure with those measured for training structures or those of simulated surface models, geometry or process parameters can be adapted and optimized. This idea has been realized for special etching surfaces e.g. in [44, 39, 40, 14].

In this paper, for the real-time extraction of the time-dependent geometrical dimensions of periodic two- and three-dimensional etch patterns, we explore scatterometric measurements, where the surface is illuminated from above and the intensity of the light scattered backward is recorded. More precisely, during a running plasma etch process we measure for each wavelength of the incoming light wave the reflected zero-order efficiency (here simply called reflectivity). Given such a spectrum of reflectivities, an inverse problem is to be solved. Indeed, a numerical algorithm is needed, which recovers the geometrical parameters responsible for the measured reflectivity spectrum.

Furthermore, since the measurement equipment provides a new spectrum nearly every second, a fast reconstruction algorithm is needed. The simulation of the reflectivity spectrum by rigorous Maxwell solvers is well established (cf. the references in Sects. 3 and 4). Unfortunately, the use of simulations is time consuming since separate time harmonic computations for each wavelength of the spectrum are required. In addition, the inverse algorithm requires simulations for several surfaces (cf. Sect. 5), which increases the time of computation significantly. To avoid lengthy computations, the following approach is suggested: Before the etching process starts, a library should be assembled. This library should contain the spectra corresponding to vectors of geometry parameters scanning the range of possible values for the geometrical parameters. Replacing the numerical simulations in the reconstruction algorithm by interpolating reflection spectra from the library, computing times less than a second are to be expected. Unfortunately, a uniform scanning of five or more parameters leads to a huge number of spectra in the library. Hence, the assembling of the library takes too long and the storage capacity might be insufficient. This phenomenon is called curse of dimension, and one approach to circumvent it is to use sparse grids for the library and the corresponding interpolation. Altogether, with a precomputed sparse-grid library, with spectra interpolated from this library, and with classical inverse algorithms an appropriate algorithm can be implemented. The aim of this paper is to demonstrate that such an approach is possible in a real plasma etch process.

The etching process considered for our numerical tests is described in Sect. 2. In Sect. 3 the mathematical model based on the time-harmonic Maxwell equations is introduced. Though, for the readers convenience, all formulas for the mathematically exact boundary value problem are presented, these details can be skipped at the first reading. The numerical approximation follows in a verbose description in Sect. 4. A few numerical spectra are compared with measured data. The details of the inverse problem for the scatterometric measurement of the geometry parameters are presented in Sect. 5. A sensitivity analysis to design an optimal library and an optimal inverse solver is discussed in Sect. 6. For the reduction of the library, a sparse-grid approach is introduced in Sect. 7. Finally, Sect. 8 exhibits numerical results of the reconstruction algorithm, and conclusions are drawn in Sect. 9. Note that most of the details are presented for the case of two-dimensional line-space structures. A generalization to biperiodic structures (crossed gratings), however, should be straightforward.

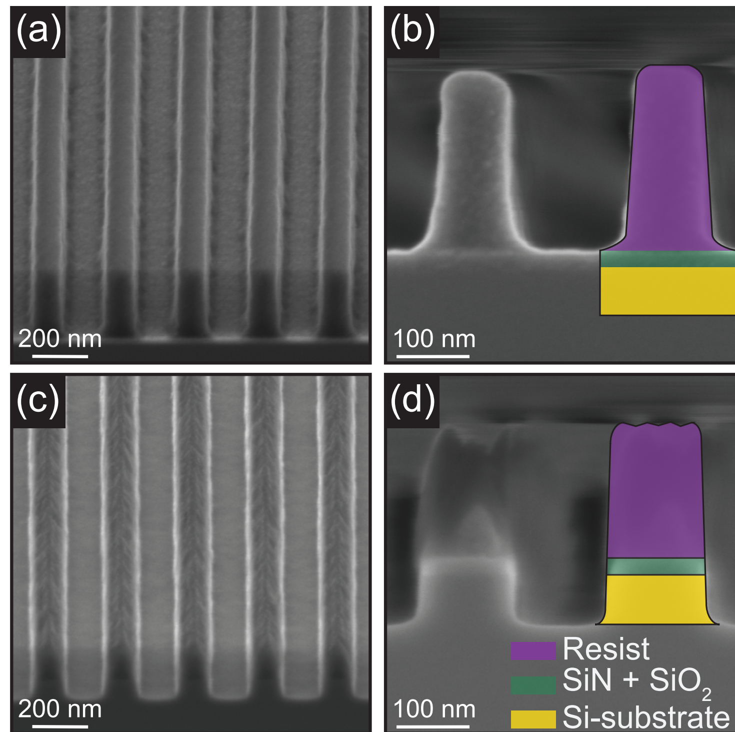

Figure 1: Tilted (left) and cross-sectional (right) SEM images of lithographic mask structure: prior RIE in Figs. (a),(b), after RIE in Figs. (c),(d).

2 Plasma etching and real-time reflectivity measurements of 2D and 3D periodic model structures

For the development of a reconstruction algorithm based on reflection spectra interpolated from the library, we first acquired a set of experimental reflectivity spectra during the etching process of two-dimensional patterns on a silicon (Si) substrate. Exemplarily, periodic line-space structures with trapezoidal multi-layer terraces in p-type (Boron) doped Czochralski (CZ) Si (100) with a resistivity of 9 – 18 Ω cm were fabricated. This process was based on standard 130 nm SiGeC BiCMOS processing steps, which are available in the pilot line of IHP (Leibniz-Institute for innovative microelectronics).

In Fig. 3, we present tilted and cross-sectional scanning-electron microscope (SEM) images prior and after the RIE process including schematics of the film structure and geometry parameters. First a lithographic mask is provided by a combination of a thin hardmask (2.0$\pm$0.1) nm SiO_2 and (20.5$\pm$0.5) nm SiN_x and a thicker photomask (ca. 300 nm). A periodic two-dimensional line pattern is temporarily formed in the photomask. Before etching, these line structures have a width of (105$\pm$10) nm and are separated by (145$\pm$10) nm (see Figs. 3(a) and (b)).

In order to test our developed reconstruction algorithm for the geometrical parameters of plasma etched structures from experimental reflectivity spectra taken during the etch process, we equipped an etching system from SENTECH (SI 591 compact) with an optical measurement system from LayTec (EpiR 2003-011). For all etch processes discussed in this paper, highly anisotropic etching was achieved using a CHF_3 (10 sccm)/CF_4 (1:4) gas mixture with 50 sccm, 50 W and 2.5 Pa as the

etch conditions.

Via a quartz viewport, optical access to the substrate surface during the plasma etch is provided, enabling the measurement of reflection spectra throughout the etch process. The measuring head covers a spectral range from 300 to 700 nm with a spectral resolution of 2.3 nm. For an optimal signal-to-noise ratio the integration time was set to 800 ms, providing at least one spectral measurement per second. Within an optimal window of 350-650 nm we achieved a total measurement uncertainty between nominal identical etch runs of 0.5$\%$. Most importantly, the generated plasma has no influence on our reflectivity measurements, as is shown in the R spectra of Figs. 3 (c) and (d) taken immediately before and after the plasma etch was started.

In the last part of this paragraph, we shall discuss the geometrical parameters relevant for the reconstruction of our exemplary two-dimensional periodic line structures. Note, in a full CMOS-fabrication process after plasma etching the lithographic mask is removed and, hence, neither the hard- or photomask are part of the final etched structure. However, for the simulation, also the permanent removal of the etch mask must be taken into account. Before the lithographic pattern is etched into the Si substrate, first the thin hardmask is opened. In the real-time analysis of the reflectivity measurements this first phase of the etch process may be neglected. Using the etch parameters listed above, on our test samples this first phase takes about 45 s. Finally, the general surface geometry in the plasma-etching process representing is a symmetric line-space structure. The cross section of the terrace is a stack of trapezoids with corner rounding at the top and at the bottom. The geometrical parameters describing this geometry are (cf. Fig. 2):

- p_0: Period of grating in x_1 direction.
- p_1: Radius of corner rounding at upper edges.
- p_2: Height of resist part in the upper of the terrace.
- p_3: Height of lower part of terrace consisting of SiN, SiO_2, and Si.
- p_4: Height of SiN part of terrace.
- p_5: Height of SiO_2 part of terrace.
- p_6: Radius of corner rounding at lower edges (footing).
- p_7: Width of terrace measured at top neglecting the corner rounding.
- $\tilde{p}_8$: Width of terrace measured at bottom neglecting the corner rounding.
- $\tilde{p}_9$: Width of terrace measured at bottom of resist part.

To get a more stable reconstructions of the parameters in an inverse algorithm, the parameters $\tilde{p}_8$ and $\tilde{p}_9$ are substituted by the average width $p_8 := (\tilde{p}_8 + \tilde{p}_9)/2$ and the halved deviation $p_9 := (\tilde{p}_8 - \tilde{p}_9)/2$ of the widths $\tilde{p}_8$ and $\tilde{p}_9$. The side-wall angles can be derived from these parameters. For instance, the side-wall angle of the upper resist part is given by $\arctan(p_2/[(\tilde{p}_9 - p_7)/2])$.

3 Mathematical model

A good model (cf. [30, 28, 42]) for the diffraction of polarized light beams by grating structures is the diffraction of planar waves by a periodic structure along the plane of all $\vec{x} := (x_1, x_2, x_3)^\top \in \mathbb{R}^3$ with $x_3 = 0$. The geometry (cf. Fig. 3) and the material distribution in $\mathbb{R}^3$ is described by the magnetic permeability μ and the electric permittivity ϵ depending on $\vec{x}$. In many optical situation, $\mu > 0$ is constant and ϵ is a piecewise constant complex valued function on $\mathbb{R}^3$ with $\epsilon(\vec{x}) > 0$ or $\Im\mathrm{m}\, \epsilon(\vec{x}) > 0$. This function ϵ is supposed to be independent of x_2 and periodic w.r.t. x_1, i.e.

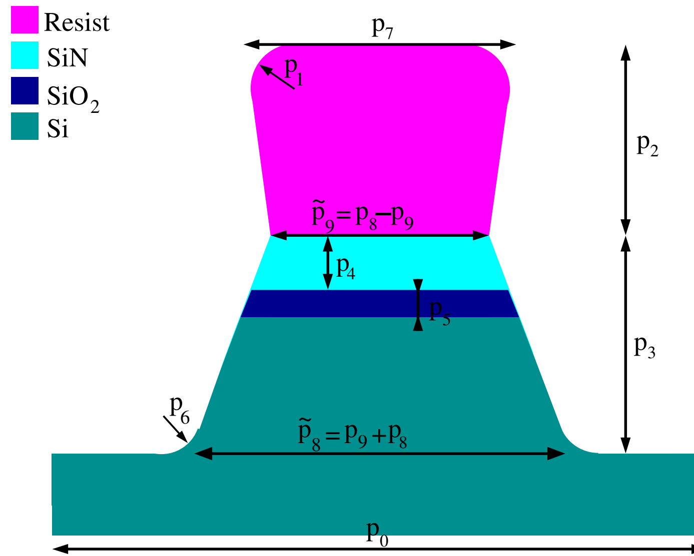

Figure 2: Geometry parameters of line-space structure for the etching process, cross section in x_1-x_3 plane over a single period in x_1 direction.

$$\epsilon\big((x_1+p_0,x_2,x_3)^\top\big) \;=\; \epsilon\big((x_1,x_2,x_3)^\top\big) \;=\; \epsilon\big((x_1,0,x_3)^\top\big)$$

holds for all points $(x_1,x_2,x_3)^\top$ and a fixed period p_0. Moreover, it can be assumed that an upper half space and lower half space is occupied by the same material. In other words, there exist constants $\epsilon^\pm$ with $\epsilon^+>0$ and numbers $x_3^\pm$ with $x_3^- < x_3^+$ such that $\epsilon(\vec{x}) = \epsilon^+$ for all $\vec{x}$ with $x_3 > x_3^+$ and $\epsilon(\vec{x}) = \epsilon^-$ for all $\vec{x}$ with $x_3 < x_3^-$.

For a given wavelength λ and the speed of light c, the electric and magnetic fields are given by $\vec{\mathcal{E}}(\vec{x},t) = \Re\mathrm{e}\, \vec{E}(\vec{x}) \exp(-\mathbf{i}\omega t)$ and $\vec{\mathcal{H}}(\vec{x},t) = \Re\mathrm{e}\, \vec{H}(\vec{x}) \exp(-\mathbf{i}\omega t)$ with $\omega := 2\pi c/\lambda$ and $\vec{E}$ and $\vec{H}$ independent of x_2 satisfying the time-harmonic Maxwell equations

$$\begin{aligned} \nabla\times\vec{E} &= \mathbf{i}\omega\vec{B}, && (1)\\ \nabla\times\vec{H} &= -\mathbf{i}\omega\vec{D}, && (2)\\ \vec{D} &= \epsilon\vec{E}, && (3)\\ \vec{B} &= \mu\vec{H}. && (4) \end{aligned}$$

Applying the curl operator $\nabla\times$ to (1) and using (2)-(4), one arrives at the equation

$$\nabla\times\nabla\times\vec{E} - k^2\vec{E} \;=\; 0, \quad k \;:=\; \sqrt{\epsilon\mu}\,\omega, \tag{5}$$

where $\Re\mathrm{e}\,k \geq 0$ and $\Im\mathrm{m}\,k \geq 0$. Due to the periodicity and due to the x_2-independence of the geometry and of the inciting incoming wave (cf. first term on the right-hand side in (9)), the field $\vec{E}$ is periodic s.t.

$$\vec{E}\big((x_1+p_0,x_2,x_3)^\top\big) \;=\; \vec{E}\big((x_1,0,x_3)^\top\big)\,. \tag{6}$$

Since on a surface only the tangential components of the electro-magnetic field are meaningful, the periodicity condition over the periodicity cell $0 < x_1 < p_0$ means

$$\begin{aligned} (1,0,0)^\top\times\vec{E}(0,x_2,x_3) &= (1,0,0)^\top\times\vec{E}(p_0,x_2,x_3), && (7)\\ (1,0,0)^\top\times\Big[\nabla\times\vec{E}(0,x_2,x_3)\Big] &= (1,0,0)^\top\times\Big[\nabla\times\vec{E}(p_0,x_2,x_3)\Big]\,. && (8) \end{aligned}$$

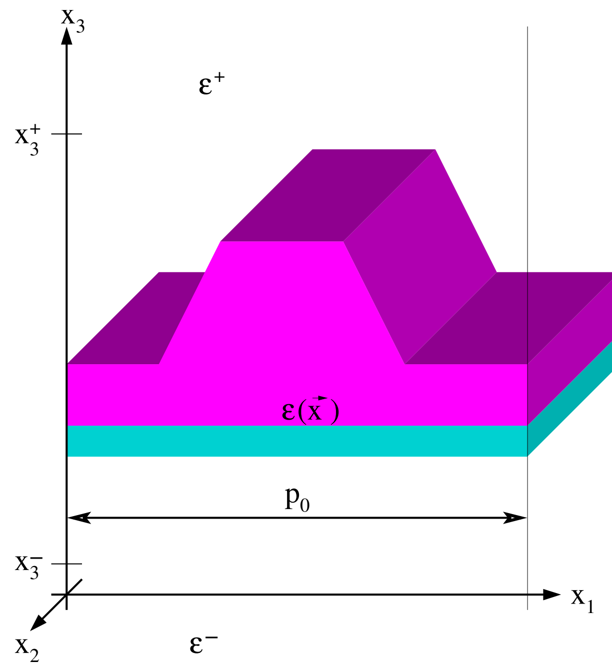

Figure 3: Geometry determined by ϵ, section over a single period.

According to the radiation condition, the field $\vec{E}$ in the upper half space $x_3 > x_3^+$ is the sum of the incoming plane wave and of up-going wave modes, i.e.

$$\vec{E}(\vec{x}) = \begin{pmatrix} r_{TM} \\ r_{TE} \\ 0 \end{pmatrix} e^{-\mathbf{i}k^+x_3} + \sum_{j=-\infty}^{\infty} \left\{ r_{TE,j}^+ \begin{pmatrix} 0 \\ 1 \\ 0 \end{pmatrix} + r_{TM,j}^+ \begin{pmatrix} 0 \\ 1 \\ 0 \end{pmatrix} \times \frac{\vec{k}_j^+}{\|\vec{k}_j^+\|} \right\} e^{\mathbf{i}\vec{k}_j^+ \cdot \vec{x}}, \quad (9)$$

where $k^+ := \sqrt{\epsilon^+\mu}\,\omega$ and $\vec{k}_j^+ := (\alpha_j, 0, \beta_j^+)^\top$ with $\alpha_j := \frac{2\pi}{p_0}j$ and $\beta_j^+ := \{[k^+]^2 - \alpha_j^2\}^{1/2}$ for $|\alpha_j| \le k^+$ and $\beta_j^+ := \mathbf{i}\{\alpha_j^2 - [k^+]^2\}^{1/2}$ else. The first term on the right-hand side describes the incoming wave, and the unknown complex valued coefficients $r_{TE,j}^+$ and $r_{TM,j}^+$ are the Rayleigh coefficients of the reflected TE and TM modes, respectively. Note that, changing the sign before the imaginary unit $\mathbf{i}$ in the exponentials of the sum, would provide us with another solution of the Maxwell equations, namely a superposition of down-going wave modes. More precisely, these modes are downwards propagating plane-wave modes or wave modes exploding to infinity for $x_3 \to \infty$. Condition (9), however, means that besides the single incoming plane-wave mode before the sum there is no further down-going mode contributing to the field. Analogously to the upper radiation condition (9), the field $\vec{E}$ in the lower half space $x_3 < x_3^-$ is the sum of down-going wave modes, i.e.

$$\vec{E}(\vec{x}) = \sum_{j=-\infty}^{\infty} \left\{ r_{TE,j}^- \begin{pmatrix} 0 \\ 1 \\ 0 \end{pmatrix} + r_{TM,j}^- \begin{pmatrix} 0 \\ 1 \\ 0 \end{pmatrix} \times \frac{\vec{k}_j^-}{\|\vec{k}_j^-\|} \right\} e^{\mathbf{i}\vec{k}_j^- \cdot \vec{x}}, \quad (10)$$

where $k^- := \sqrt{\epsilon^-\mu}\,\omega$ and $\vec{k}_j^- := (\alpha_j, 0, -\beta_j^-)^\top$ with $\beta_j^- := \{[k^-]^2 - \alpha_j^2\}^{1/2}$ the square root uniquely defined by $\beta_j^- > 0$ for $[k^-]^2 - \alpha_j^2 > 0$ and by $\Im m\, \beta_j^- > 0$ else. Again the unknown complex valued coefficients $r_{TE,j}^-$ and $r_{TM,j}^-$ are the Rayleigh coefficients of the transmitted modes. Note that these modes are downwards propagating plane-wave modes or wave modes fast decaying to zero for $x_3 \to -\infty$.

Altogether the field $\vec{E}$ is the solution of a boundary value problem for the partial differential equation (5) over the domain $0 \le x_1 \le p_0,\ x_3^- \le x_3 \le x_3^+$. The boundary conditions are the lateral periodicity condition (cf. (7) and (8)) and the upper and lower radiation conditions. The upper radiation condition means that there exist Rayleigh coefficients $r^+_{TE,j}$ and $r^+_{TM,j}$ such that the solution $\vec{E}$ of (5) for $x_3^- \le x_3 \le x_3^+$ restricted to the plane $x_3 = x_3^+$ coincides with the right-hand side of (9) and the trace of the curl $\nabla\times\vec{E}$ with the trace of the curl of the right-hand side of (9). Analogously, the lower condition means that there exist Rayleigh coefficients $r^-_{TE,j}$ and $r^-_{TM,j}$ such that the solution $\vec{E}$ of (5) for $x_3^- \le x_3 \le x_3^+$ restricted to the plane $x_3 = x_3^-$ coincides with the right-hand side of (10) and the trace of the curl $\nabla\times\vec{E}$ with the trace of the curl of the right-hand side of (10). Note that this classical diffraction problem splits into two uncoupled boundary value problems of similar structure for the scalar Helmholtz equation with the solutions equal to the transverse component $[\vec{E}\,]_2$ of the TE polarized solution and to the transverse component $[\vec{H}\,]_2 = \frac{1}{\mathrm{i}\omega\mu}[\nabla\times\vec{E}\,]_2$ of the TM polarized solution, respectively.

Now consider a propagating reflected and transmitted mode, i.e. suppose that $\alpha_j \le k^\pm$. If the normalization condition $|r_{TE}|^2 + |r_{TM}|^2 = 1$ holds for the incoming wave, then the TP ($TP = TE$ or $TP = TM$) efficiency $E^\pm_{TP,j}$ of the jth diffracted TP mode is given by

$$E^\pm_{TP,j} \;:=\; \frac{\beta_j^\pm [k^+]^2}{\beta_0^+ [k^\pm]^2}\, |r^\pm_{TP,j}|^2. \tag{11}$$

This is the portion of energy from the incoming light energy, which is propagated into the jth TP mode. While the directions $\vec{k}_j^\pm/\|\vec{k}_j^\pm\|$ of the diffracted modes are the same for all geometries with the same period p_0, the efficiencies depend on the geometries, i.e. on the values of $\epsilon(\vec{x})$ for $x_3^- < x_3 < x_3^+$. According to (11), the modulus of the Rayleigh coefficient contains the full information on the efficiency. Note that the quotient $r^\pm_{TP,j}/|r^\pm_{TP,j}|$ contains the information of the phase shift of the mode relative to the phase of the incoming mode. Usually, the reflectance of the grating is the sum of all reflected efficiencies of propagating plane-wave modes. However, throughout the present paper, the zero order efficiency $E^+_{TP,0}$ will be called reflectance of TP polarization since this is the value determined by devices measuring the outgoing waves in the direction opposite to that of the incoming wave.

In order to simulate unpolarized light, one should simulate many differently polarized waves and compute the efficiencies $E_j^\pm$ and the reflectances E_0^+ by averaging. In the case of periodic line-space structures, fortunately, the efficiencies are simply the averages of the TE and TM values, i.e. the reflectance is given as $E_0^+ = (E^+_{TE,0} + E^+_{TM,0})/2$.

4 Numerical simulation of reflectance spectra

For the numerical computation of the electro-magnetic fields, there exist many different Maxwell solvers. The classical mathematical approach to boundary value problems for partial differential equations would be to apply finite element (FEM) (cf. e.g. [11, 43, 1, 12, 3, 6, 7, 8, 13, 36, 37, 4, 23, 33, 22]) or boundary element methods (BEM) (cf. e.g. [26, 31, 35, 24, 45]). Very popular is also a method based on slicing the surface structure, on computing the reflection and transmission coefficients for each slice by Fourier mode expansion, and on combining the results by a stable iteration to get the global coefficients. This method is called rigorous coupled wave analysis (RCWA), Fourier modal method (FMM), or scattering matrix method (SMA) (cf. e.g. [27, 19, 25, 5, 28]). For further methods one should look e.g. at [30, 10, 41, 33]. Finally, for a fast computation method in case of a huge number of simulations, a good approach can be found in [32].

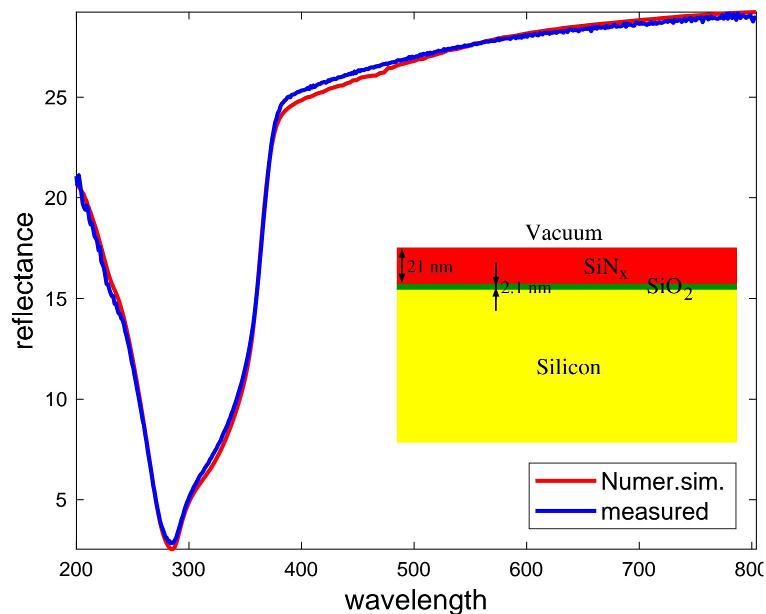

Figure 4: Spectra for a multi-layer system. SiN_x over SiO_2 over Si substrate. Comparison of numerical simulation (red line) and measured spectrum (blue line).

An abstract comparison of all these methods is difficult. Lets look, e.g. at the RCWA and the FEM. Note that the FEM is a basic discretization scheme like the Fourier mode expansion in the RCWA. So the scattering matrix iteration in the RCWA could have been combined with an FEM approximation, replacing the Fourier-mode expansion. In fact, the scattering matrix iteration is something what in the FEM community is known as domain decomposition method, but for a special kind of geometries. Consequently, instead of a theoretical comparison of FEM and RCWA, one should compare FEM and Fourier-mode expansion, and one should compare slicing and domain decomposition. Of course, the implemented program packages should be compared by numerical test. In general, it seems that the classical RCWA is very good for gratings with thick slices of geometries not depending on the x_3-direction and for non-absorbing materials. An adaptive high-order FEM seems to be a good choice, when singularities in the solution have a strong impact on the efficiencies.

The numerical results presented in this paper have been generated by the SMA, where the scattering matrix is computed by integrating the operator valued “ordinary” differential equation in x_3 direction (cf. e.g. [28]). A comparison with our FEM code has proven that the efficiencies computed by SMA are reliable. Fig. 4 shows the reflectance spectrum of a multi-layer system consisting of a silicon substrate coated with an SiO_2 layer (2.1 nm) and a silicon nitrite layer (21 nm) on top. The simulated spectrum is in good agreement with the measured spectrum. Note that the measurement data is obtained by a device of the LayTec company, which is capable to measure in-situ reflectances in etching processes.

Spectra for a line-space structure (cf. Fig. 2) with $p_0 = 264.1$ nm, $p_1 = 37.4$ nm, $p_2 = 230.2$ nm, $p_3 = 52.6$ nm, $p_4 = 20.5$ nm, $p_5 = 2.05$ nm, $p_6 = 26.5$ nm, $p_7 = 135.9$ nm, $\tilde{p}_8 = 135.9$ nm, and $\tilde{p}_9 = 133.7$ nm are shown in Fig. 5. The lines in yellow, pink, blue, and black show measured spectra for four periodic structures close to Fig. 2 with the just mentioned parameters. The geometric parameters have been checked from SEM pictures taken after interrupting the etching process of Sect. 8 after 175 s. The dashed red line is the corresponding simulated spectrum. The full red line is that of a spectrum simulated with a finer geometrical resolution, where the resist part is approximated by two

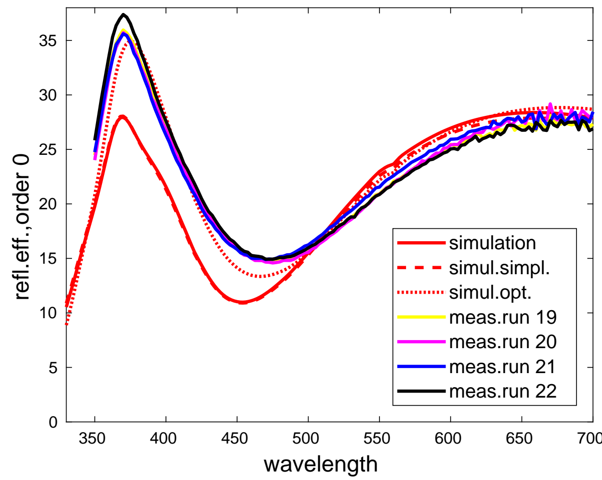

Figure 5: Spectra for a periodic line-space structure (cf. Fig. 2). Three simulated spectra (red) and four measured (yellow, pink, blue, and black).

instead of a single trapezoidal layer. Finally, the dotted red line is the simulated spectrum closest to the yellow line such that the parameters do not differ from the just mentioned values by 5 nm for heights and 10 nm for widths. Unfortunately, there is still a mismatch between simulated and measured reflectances. Probably, the estimated geometry parameters for the measured surface deviate from the true values.

The spectrum for a biperiodic grating (cf. Fig. 6) is shown in Fig. 7. The hard mask (HM) consists of an upper $\mathrm{SiO_2}$ layer (10 nm), a SiN layer (20.7 nm) in the middle, and a lower $\mathrm{SiO_2}$ layer (2.1 nm). The height of the whole conical terrace is 180 nm. The diameter of the terrace is $\mathrm{Diam} = 120$ nm at the foot. The side-wall angle is $86°$. All the pillars are allocated in a uniform rectangular scheme with the periods both equal to 255 nm. For the edges, there is a corner rounding with a radius of $r_1 = 12.5$ nm at the foot and with $r_2 = 17.5$ nm at the top. Note that without corner rounding the lower diameter is $\mathrm{diam} \approx \mathrm{Diam} - 2 \cdot r_1$, i.e. $\mathrm{diam} = 110$. Though the pillars on the measured surface are not perfectly conical, the simulated reflectances are in good agreement with the measured ones.

5 The inverse reconstruction problem

Now suppose, the surface geometry can be described by a vector of parameters $(p_j)_{j=1}^J$. Usually, some of these parameters are fixed to good estimates s.t. there remains a vector of unknown parameters $\mathbf{p} := (p_j)_{j\in\Upsilon},\ \Upsilon \subseteq \{1, 2, \ldots, J\}$ to be determined. The exact values are denoted by $\mathbf{p}^{true} := (p_j^{true})_{j\in\Upsilon}$. The measurement device manufactured by the LayTec company produces time depending reflectance spectra (cf. Fig. 8). In other words, the device provides the reflectances for the wavelengths $\lambda_k,\ k = 1, \ldots, N$, which are fixed between 350 and 700 nm.

Unfortunately, the data is noisy. If, for any vector of parameters $\mathbf{p}$ the reflectance spectrum of the corresponding geometry is denoted by $\mathbf{E}(\mathbf{p}) := (E_0^+(\lambda_k, \mathbf{p}))_{k=1}^N$, then the measurement values $\mathbf{E}^{meas} = (E_k^{meas})_{k=1}^N$ are given as

$$E_k^{meas} \quad = \quad E_0^+(\lambda_k, \mathbf{p}^{true}) + U_k^E. \tag{12}$$

Here the uncertainties U_k^E are assumed to be normally distributed random variables with zero mean

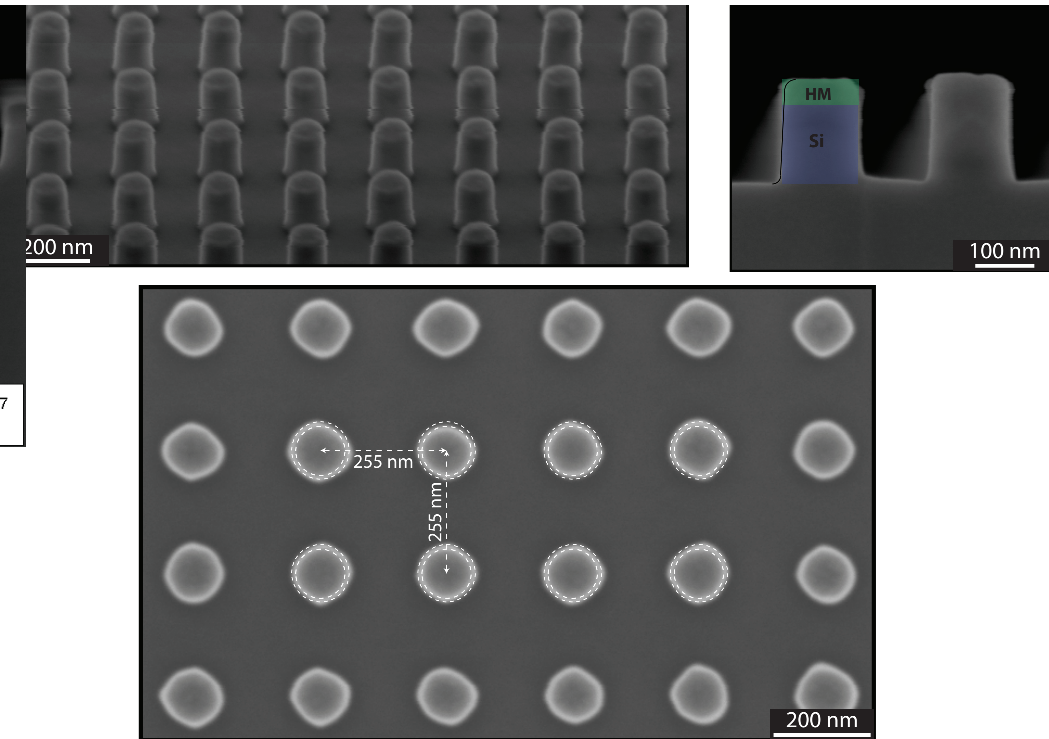

Figure 6: Geometry of a biperiodic pillar structure. Side view (above) and top view (below).

and standard deviation u_k^E, and the U_k^E for different k are supposed to be independent. Clearly, this is only a simplification of the true statistics of measurement. In particular, systematic errors are neglected. Unfortunately, due to the simple mathematical model systematic errors might occur.

To get the standard deviations u_k^E, the time dependent reflectance spectra for four almost identical etching processes have been measured (cf. Sect. 8). Then a simple statistical estimator yields a value for each wavelength and at each time step. Taking the supremum over the time steps results in Fig. 9.

Now the task in the inverse problem of scatterometry is to construct a good approximation for the vector of parameters $\mathbf{p}^{true}$ from the vector $\mathbf{E}^{meas}$. Usually, one takes the approximation $\mathbf{p}^{opt}$, for which the deviation of the measured spectrum from the spectrum corresponding to $\mathbf{p}^{opt}$ is minimal, i.e. $\mathbf{p}^{opt}$ is the solution of the non-linear optimization problem

$$\min_{\mathbf{p}=(p_j)_j:\, p_j^- \le p_j \le p_j^+} f(\mathbf{p}), \qquad f(\mathbf{p}) \;:=\; \sum_{k=1}^{N} \frac{1}{[u_k^E]^2} \left| E_k^{meas} - E_0^+(\lambda_k, \mathbf{p}) \right|^2 . \tag{13}$$

The bounds $p_j^\pm$ should be chosen reasonably. A general solution of the optimization problem (13) might be difficult. If, however, a good initial guess for the optimal solution is available, then a fast local gradient based optimization scheme can be applied. Popular are e.g. the Newton, the Gauss-Newton, the Levenberg-Marquard, and the SQP method (cf. [29, 2, 15]). In the present paper, a simple Newton method with Tikhonov regularization and the SQP of the commercial code SNOPT [15] is used. For further details, see e.g. [9]. The problem of systematic model errors is considered e.g. in [21, 17, 16]. Alternatively to the optimization problem (13), a Bayesian approach is proposed e.g. in [20].

If the standard deviations u_k^E of the normally distributed measurement uncertainties U_k^E (cf. (12)) are small, then the uncertainties of the reconstructed parameter values can be estimated by linearization.

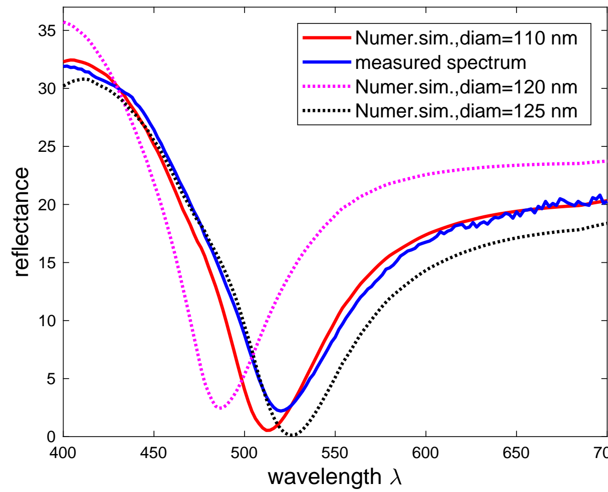

Figure 7: Spectra for a biperiodic structure (cf. Fig.6).

Setting

$$A \;:=\; (a_{j,k})_{\substack{j\in\Upsilon\\ k=1,\dots,N}} \;:=\; [B^*B]^{-1}\,B^*, \quad B \;:=\; \left[\left(\frac{\partial E_0^+(\lambda_k,\mathbf{p}^{true})}{\partial p_j}\right)_{k,j}\right]^{-1},$$

results in $p_j^{opt} \approx p_j^{true} + U_j^p$ with $U_j^p := \sum_k a_{j,k} U_k^E$. Taking into account that the U_k^E for different k are independent, a simple estimate for the standard deviations u_j^p can be derived by

$$u_j^p \;\approx\; \sqrt{\sum_{k=1}^{N} [a_{j,k} u_k^E]^2}. \tag{14}$$

This estimate of the uncertainty for the reconstructed parameter values is nothing more than a lower estimate since non-linear higher order terms, more complex measurement-uncertainty models, and systematic model errors have been neglected.

In applications to etching processes, a time-dependent process must be traced. Every second a new measured spectrum is generated, for which the geometry parameters are to be determined. Since the parameters do not change too fast in the etching process, the optimal solution from the previous time step is a good initial guess for the actual optimization. In the very beginning, the optimal solution is known. E.g. the process might start with the geometry of a simple multi-layer system covered by resist lines.

6 Sensitivity analysis to fix the adequate parameters

Before switching to the implementation of the inverse problem, which recovers the geometry parameters from the reflectance spectra, it is useful to check, which of the parameters has an important effect on the spectrum. Therefore, relevant examples of the geometry should be taken, the parameters should be changed, and the corresponding spectra should be plotted. E.g. the geometry with optical indices $n + ik := \sqrt{\epsilon/\epsilon^+}$ given in Fig. 10 describes a surface of the etching process in Sect. 8 after 100 s. The period p_0 and the heights $p_j,\;\; j = 4, 5$ remain constant during the etching and can

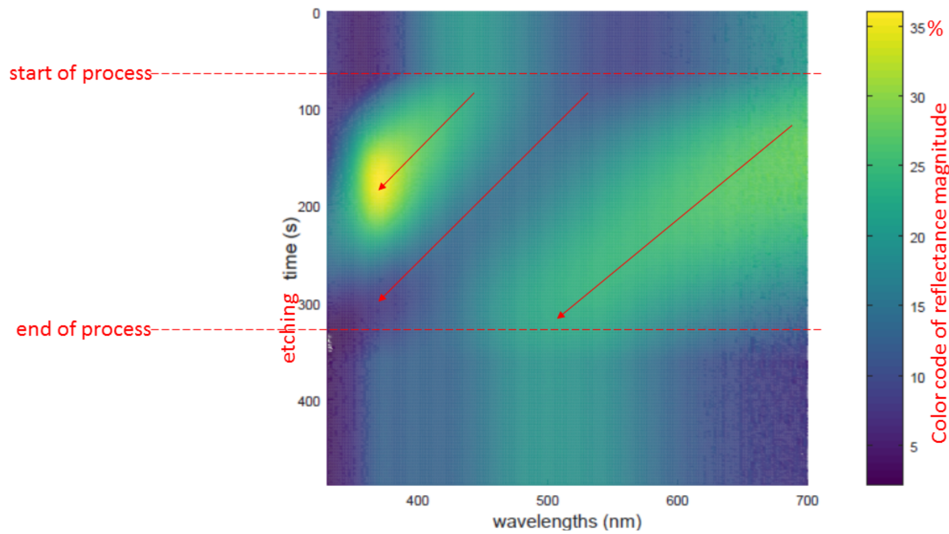

Figure 8: Typical reflectance plot of a Laytec device for an etching process. Reflectance in $\%$. Each second a new spectrum is taken and color-coded for real-time visualization.

be assumed to be known. For a slight change of the other parameters, the spectra of the Figs. 11 –14 can be simulated.

The spectra remain almost unchanged for variations of the period and the radii of corner roundings. A reconstruction of such parameters might be a hard task. Therefore, the parameters p_0, p_1, and p_6 are fixed to an approximate value. For the geometry reconstruction, it remains to recover the parameters $p_j,\ j \in \Upsilon := \{2,3,7,8,9\}$ (cf. Fig. 2).

From the view point of statistics, it would be good to reconstruct from as many wavelengths as possible, i.e. to choose a large N. A scanning of the range from 350 nm to 700 nm in steps of 2 nm would be possible. However, in order to reduce the computing time for the generation of the library, the number of chosen wavelengths is reduced to $N=16$. Now the question arises, which wavelengths should be taken. Note that, if N should be increased to take care of measurement uncertainty, then one should rather apply a smoothing to the measured spectrum and, afterwards, restrict the smoothed spectrum to a spectrum over a smaller set of wavelengths.

To get the wavelengths, the sensitivity analysis of [18] can be applied. The starting point is a scanning of the range to get $\tilde{\lambda}_k := 350$ nm$+k \cdot 2.5$ nm, $\ k=0,\ \dots\ ,140$. Then the Jacobian matrix

$$\mathcal{J} := \left(\frac{1}{u_k^E} \frac{\partial E_0^+(\tilde{\lambda}_k, \mathbf{p})}{\partial p_j} \right)_{\substack{k=0,\dots,140 \\ j \in \Upsilon}} \tag{15}$$

is computed with the uncertainty estimates u_k^E from the beginning of Sect. 5. Now for any subset $\Lambda := \{\lambda_k : \ k=1,\ \dots\ ,N\}$ of the full grid $\{\tilde{\lambda}_k : \ k=0,\ \dots\ ,140\}$ containing the five wavelengths $(405+l \cdot 60)$ nm, $\ l=0,\ \dots\ ,4$, the corresponding submatrix of $\mathcal{J}$ is denoted by $\mathcal{J}_\Lambda = \mathcal{J}_\Lambda(\mathbf{p})$. The better the conditioning of the matrix $\mathcal{J}_\Lambda(\mathbf{p})$, the better is the reconstruction of the parameters from the reflectivities over wavelengths of Λ, if the parameters are close to the components of the vector $\mathbf{p}$. In order to get good reconstructions for the measurements of the geometrical parameters varying during the etching, a collection of representative parameter vectors $\mathbf{p}^m$, $m=1,\ \dots\ ,M$ is chosen and the optimal Λ is determined minimizing, instead of a single condition number, the worst conditioning of the $\mathcal{J}_\Lambda(\mathbf{p}^m),\ m=1,\ \dots\ ,M$. In other words, the eleven missing wavelengths for the sixteen wavelengths

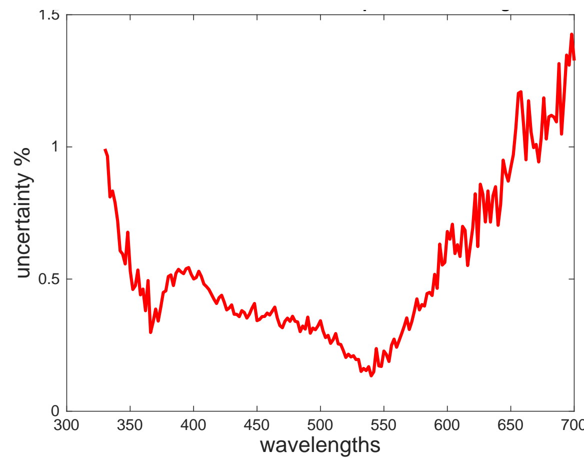

Figure 9: Uncertainties depending on the wavelength. Absolute values for reflectivity given in per cent. Derived from estimators for four almost identical etching processes.

of Λ should be chosen such that the maximum

$$\max_{m=1,\dots,M} \mathrm{cond}\Big([\mathcal{J}_\Lambda(\mathbf{p}^m)]^* \, \mathcal{J}_\Lambda(\mathbf{p}^m)\Big)$$

is minimal, where the condition number cond is the quotient of maximal eigenvalue over minimal eigenvalue. However, since the number of submatrices is too big, the subset Λ of the 140 wavelengths is to be determined by a greedy search algorithm (cf. [18]).

Applying the above optimization to the reconstruction process of Sect. 8 with $M=6$ and the parameter vectors $\mathbf{p}^m$ chosen as the values of the etching process after 80, 100, 125, 150, 175, and 200 seconds, the algorithm leads to the set in Fig. 15. Though the uncertainties for small and big wavelengths are larger, the optimal set Λ contains many small and big wavelengths.

7 Sparse grid interpolation

For a fast numerical reconstruction of the geometry parameters from the measured spectra, a numerical simulation is too slow. Note that the time of simulation is to be multiplied by the number of wavelengths, the number of polarizations, and the number of iteration in the optimization algorithm. Therefore, the simulation should be replaced by an interpolation of spectra stored in a huge library. The library can be computed before the etching and measurement process is started, and the assembling of the library may take a longer time.

If $1+2^4=17$ values are used to scan a single parameter at the equidistant interpolation knots of level four, then the full tensor product grid for the scanning of the five-dimensional space of parameter vectors consists of $1\,419\,857$ points. For spectra of 16 wavelengths and two polarizations, this means $45\,435\,424$ simulations and a storage capacity of 182 MB. Using sparse grid interpolation [38], this can be reduced to a number of $2\,852$ points, to $91\,264$ simulations and to a storage of 0.365 MB. Indeed, for the level $L=4$, the set of all full grid points $\mathbf{p}$ s.t.

$$\mathbf{p} = \left(p^L_{j,m}\right)_{j\in\Upsilon}, \quad p^L_{j,m} \;:=\; p^-_j + [p^+_j - p^-_j]\,\frac{m}{2^L}, \quad m=0,\,\dots\,,2^L$$

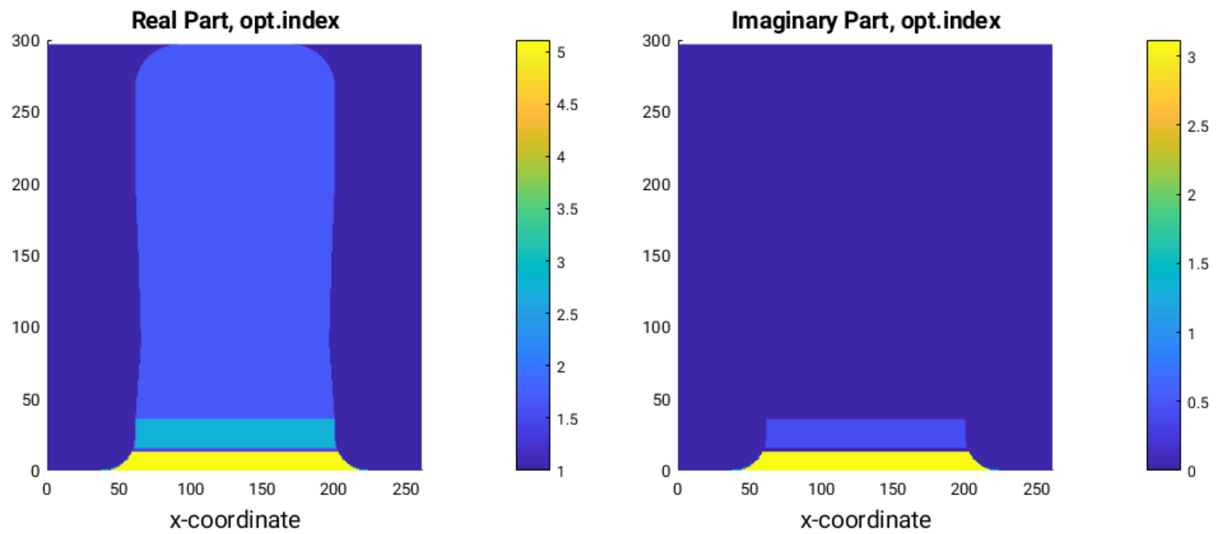

Figure 10: Optical index for a surface structure over the period taken from an etching process after 100 s.

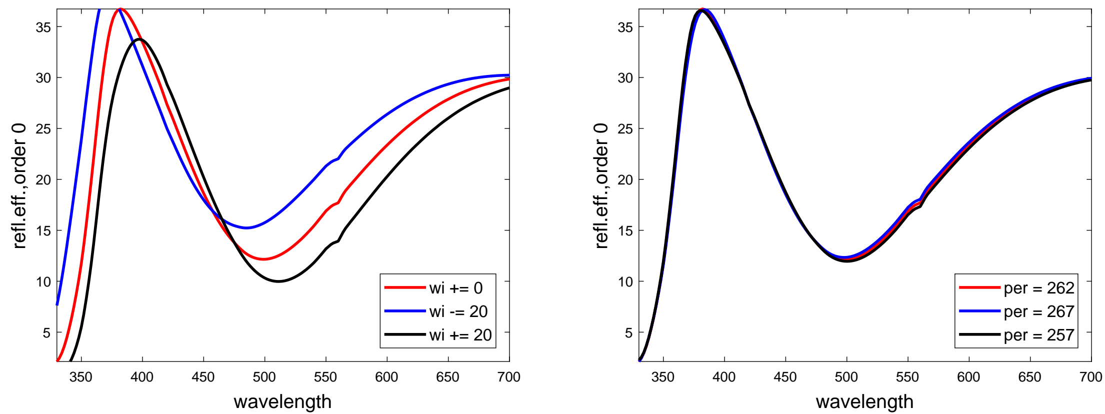

Figure 11: Spectra for geometry of Fig. 10 with varying terrace width in nm (left) and period in nm (right).

can be replaced by the set of all sparse grid points $\mathbf{p} = (p^{l_j}_{j,m_j})_{j\in\Upsilon}$ such that $m_j = 0,\ldots,2^{l_j}$ and $\sum_{j\in\Upsilon} l_j \leq L$. Denoting the interpolation onto a general space of approximate functions, defined over the level l points in the jth dimension with $j \in \Upsilon = \{k_1, \ldots, k_v\} \subseteq \{1, \ldots, J\}$, by

$$P^l_j f(p_j) = \begin{cases} \sum_{m=0}^{2^l} f\left(p^l_{j,m}\right) \varphi^l_{j,m}(p_j) & \text{if } l=0, \ldots, L \\ 0 & \text{else} \end{cases} \tag{16}$$

and introducing the difference projector

$$\begin{aligned} P^l_j f(p_j) - P^{l-1}_j f(p_j) &= \sum_{m=0}^{2^l} f\left(p^l_{j,m}\right) \psi^l_{j,m}(p_j), \quad l=0, \ldots, L, \\ \psi^l_{j,m}(p_j) &:= \begin{cases} \varphi^l_{j,m}(p_j) - \varphi^{l-1}_{j,m/2}(p_j) & \text{if } m \text{ even} \\ \varphi^l_{j,m}(p_j) & \text{else} \end{cases}, \end{aligned}$$

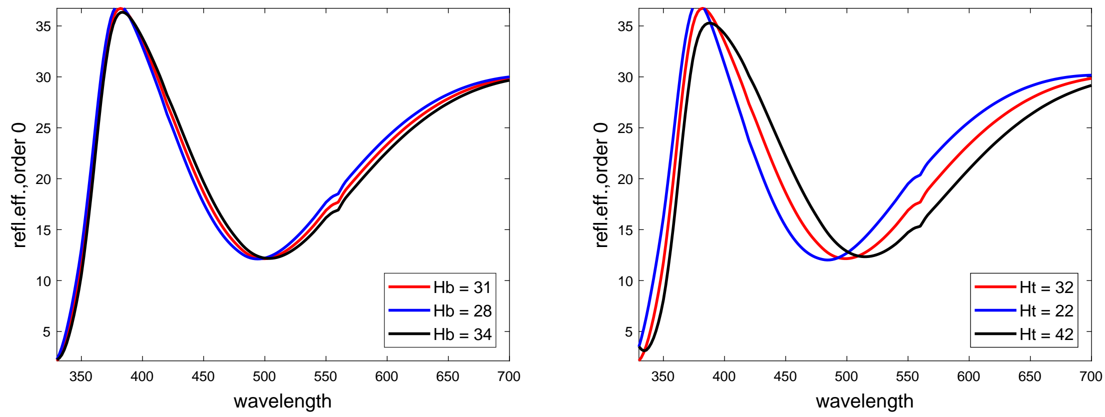

Figure 12: Spectra for geometry of Fig. 10 with varying heights of the silicon layer in nm (left) and the photo-resist layer in nm (right).

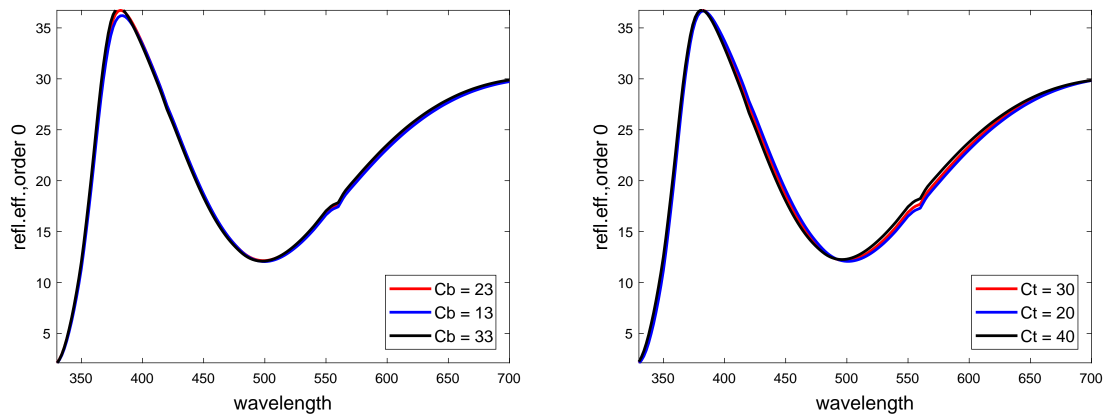

Figure 13: Spectra for geometry of Fig. 10 with varying radius of lower corner rounding in nm (left) and upper corner rounding in nm (right).

the full tensor-product interpolation

$$F(\mathbf{p}) \quad \sim \quad \sum_{m_1=0}^{2^L} \dots \sum_{m_v=0}^{2^L} F(p^L_{k_1,m_1}, \, \dots \, , p^L_{k_v,m_v}) \, \varphi^L_{k_1,m_1}(p_{k_1}) \, \dots \, \varphi^L_{k_v,m_v}(p_{k_v})$$

is replaced by the sparse grid interpolation

$$F(\mathbf{p}) \sim \sum_{\substack{\forall l_j \geq 0, \, j=1,\dots,v: \\ l_1 + \dots + l_v \leq L}} \sum_{m_1=0}^{2^{l_0}} \dots \sum_{m_v=0}^{2^{l_v}} F(p^{l_1}_{k_1,m_1}, \, \dots \, , p^{l_v}_{k_v,m_v}) \, \psi^{l_1}_{k_1,m_1}(p_{k_1}) \, \dots \, \psi^{l_v}_{k_v,m_v}(p_{k_v}). \quad (17)$$

The interpolation P^l_j in (16) could be an interpolation onto trigonometric or spline functions. In the present paper, the interpolation mapping onto the space of continuous cubic splines is used, which results in local basis functions $\psi^l_{k,m}$.

Note that sparse grid interpolation requires more smoothness than the full grid interpolation. In our application, however, the reflectance functions $\mathbf{p} \mapsto E^+_0(\lambda, \mathbf{p})$ can be assumed to be smooth. This

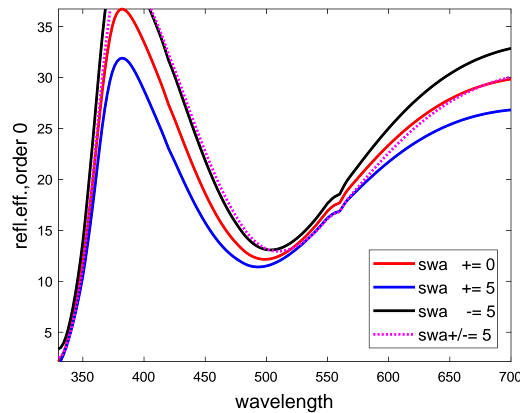

Figure 14: Spectra for geometry of Fig. 10 with varying side-wall angle in degrees. Dotted pink line corresponds to side-wall angle varied by 5° in a lower and upper part and by -5° in the middle.

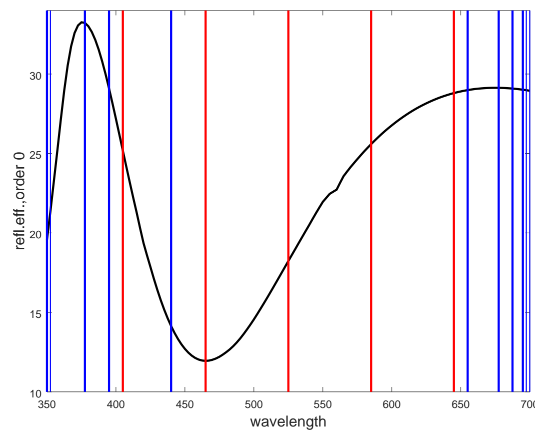

Figure 15: Computed spectrum and "optimal" wavelengths for the inverse algorithm indicated by vertical lines. Red lines are the 5 wavelengths fixed a priori. Blue lines are the 11 new wavelengths obtained by optimization for the geometry of the etching process (cf. Sect. 8).

is to be expected for differential families of geometries. Note that such families are defined by the permittivity functions $\epsilon_{\mathbf{p}}(\vec{x}) = \epsilon_0(\Phi_{\mathbf{p}}(\vec{x}))$ with ϵ_0 the permittivity function of a fixed geometry and $\Phi_{\mathbf{p}}$ a diffeomorphic family of mappings $\mathbb{R}^3 \to \mathbb{R}^3$, depending on the parameter vector $\mathbf{p}$. In particular, subdomains of the fixed geometry made of the same material with constant permittivity $\epsilon_0 = \epsilon_{\text{const}}$ are mapped diffeomorphically to subdomains with $\epsilon_{\mathbf{p}} = \epsilon_{\text{const}}$ of the same material. However, if the time dependent geometry is changed qualitatively such that new subdomains with different ϵ values arise or old ones disappear, then the reflectance function is continuous but might be not differentiable. This happens if the etching process is entering a new material layer. In this case, the set of parameter vectors $[p_{k_1}^-, p_{k_1}^+] \times \ldots \times [p_{k_v}^-, p_{k_v}^+]$ should be split, and over each parameter subset a separate sparse-grid library should be generated.

An example of the reflectance and its level four sparse-grid interpolation error is shown in Fig. 16. This is the sparse grid of the library for the process considered in Sect. 8. Here the fixed parameters of Fig. 2 given in nm are $p_0 = 261.6$, $p_1 = 32.3$, $p_4 = 20.5$, $p_5 = 2.05$, $p_6 = 25.1$, $p_7 = 135.5$, $p_8 = 135.4$,

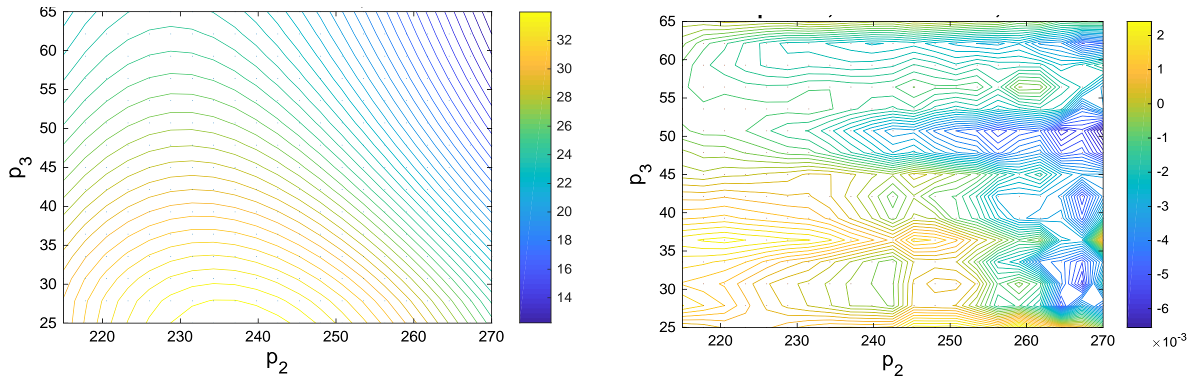

Figure 16: Reflectance for wavelength of 350 nm (left) and level 4 sparse-grid interpolation error (right).

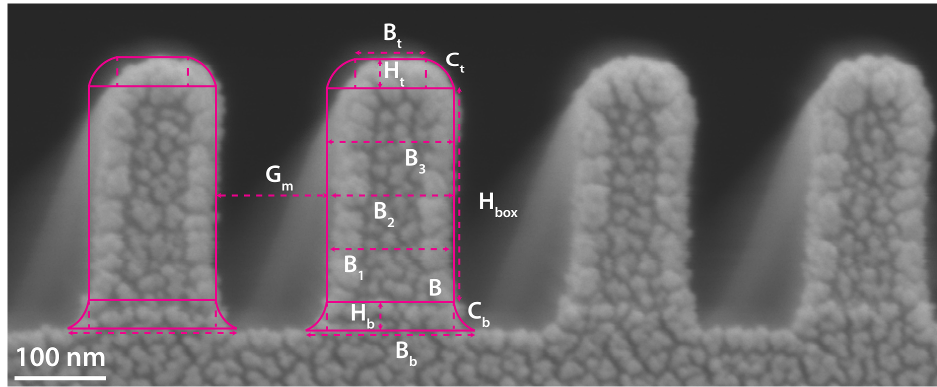

Figure 17: Crosssectional SEM picture of a line-space surface structure after 100 s of the etching process. Prior to the SEM the sample was coated with about 1 nm of Au to avoid charging effects whilst imaging the resist.

and $p_9 = 0.14$. The bounds $p_j \in [p_j^-, p_j^+]$ of the box for the sparse-grid interpolation are given as

$$p_2 \in [215, 270], \quad p_3 \in [25, 65], \quad p_7 \in [125, 150], \quad p_8 \in [125, 150], \quad p_9 \in [0, 10]. \tag{18}$$

Using appropriate discretization parameters, the library has been computed on 32 CPUs in 55.34 min (HP BL460c Gen8, 2xXeon, Eight-Core 2700 MHz, 128 GB RAM). Note that a library computation for more parameters or for a complex biperiodic geometry can take a much longer time. On the other hand, an adaptive choice of the sparse grid can save time and storage capacity.

8 Numerical reconstruction of a plasma-etching process

Now the reconstruction algorithm of Sect. 5 is applied to the etching process of Sect. 2 and to simulated data for the reflectance spectra. The vector of true parameter values is time dependent, i.e. $\mathbf{p}^{true} = \mathbf{p}^{true}(t),\ \ 80\,s \leq t \leq 200\,s$. Note that after $80\,s$ the etching has reached the Si layer, the surface geometries of the etching process are all diffeomorphic, and the $\mathbf{p}^{true}(t)$ is in the domain like (18), where the reflectivity is a smooth function of $\mathbf{p}$. The values $p_0 = 261.6$ nm, $p_1 = 32.3$ nm, $p_4 = 20.5$ nm, $p_5 = 2.05$ nm, and $p_6 = 25.1$ nm are fixed. To get the remaining parameters, five identical etching processes have been performed but interrupted after 80, 100, 125, 150, 175, and 200

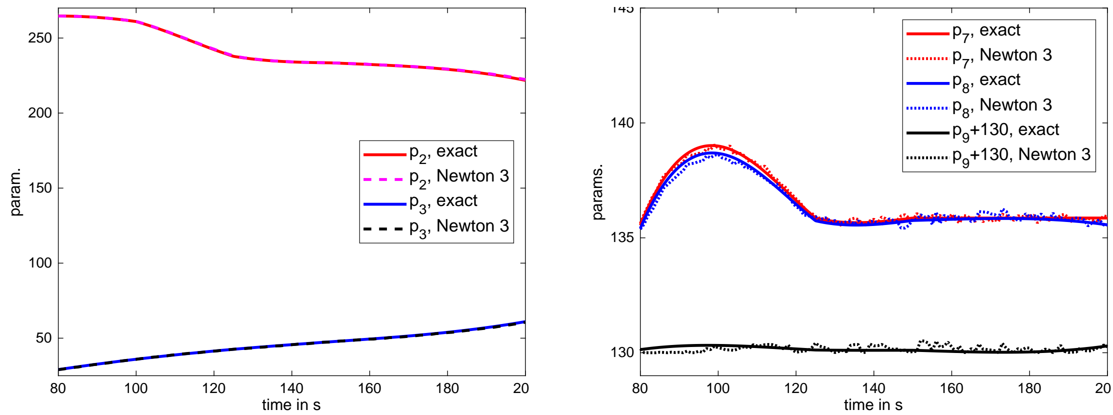

Figure 18: Exact and reconstructed parameters p_2 and p_3 (left) and p_7, p_8, and p_9 (right) for measurement data with $\sigma = 0.02$.

seconds. Then the geometry parameters have been measured using SEM (cf. e.g. Fig. 17). Finally, the parameters are interpolated to obtain the values of the continuous lines in Fig. 18. The interpolation scheme is piecewise cubic. However, to get monotone functions p_2^{true} and p_3^{true} the interpolation scheme for times less than 125 s is changed into a linear combination of linear and cubic interpolation.

For our numerical experiment time dependent measurement data has been simulated. Fixing a perturbation level σ, the measured efficiency values are chosen as $E_k^{meas}(t) = E_0^+(\lambda_k, \mathbf{p}^{true}(t)) + \sigma \cdot U_{t,k}^E$ with uniformly distributed random numbers $U_{t,k}^E \in [-1, 1]$, which are independent for different t and k. The restrictions for the search algorithm solving (13) are the same as for the scanning, namely those of (18). However, using the a-priori information on the monotonicity, the upper bound p_2^+ and the lower bound p_3^- have been set to the values of the last time step p_2 and p_3, respectively. Next, the reconstruction algorithm is to be adapted to the geometries corresponding to the restrictions (18) and to the uncertainty level σ. For instance in case of the Newton algorithm, the maximal number of iterations and the regularization parameter is to be adapted. Note that in each Newton step a vector equation with the Hessian matrix is to be solved. Since this is ill-conditioned, a Tikhonov regularization with fixed regularization parameter is to be applied. In all reconstructions, no more than 3 iterations have been applied. Finally, the results of the reconstruction for perturbation level σ equal to 0.02, 0.1, and 0.5 are shown in the Figs. 18, 19, and 20, respectively. The depth parameters p_2 and p_3 are well reconstructed from the measurements. The smaller the measurement uncertainty σ the better the reconstruction. Unfortunately, the approximate values for the widths p_7 and p_8 differ from the correct values. For $\sigma \leq 0.1$ the curve of the time-depending approximate values still follows the shape of the curve of true values. The reconstruction of the difference width p_9, however, is poor even for $\sigma = 0.02$. Note that the error estimates (14), based on the estimated measurement uncertainties u_k^E in Fig. 9 and not on the σ, suggest a reconstruction uncertainty for $p_j,\ j = 2, 3, 7, 8, 9$ equal to 1.4, 3.9, 7.0, 10.2, and 12.0 nanometers, respectively.

Looking at the continues curves in Fig. 18, the width of the terrace is almost independent of the x_3-coordinate and of the time of the etching process. Therefore, in a final test the widths p_7 and p_8 are fixed to the estimated value of 135 nm and p_9 to 0. Applying the algorithm to the reconstructions of the depth parameters, leads to the plot on the right of Fig. 21. The reconstructed parameter p_3 is slightly worse than that of the algorithm including the search for p_7, p_8, and p_9 on the left of Fig. 21.

Of course, in all cases, the computing time is smaller than the time of the etching process. For example, the reconstruction by Newton iteration with the results in Fig. 19 requires about 0.03 seconds, while

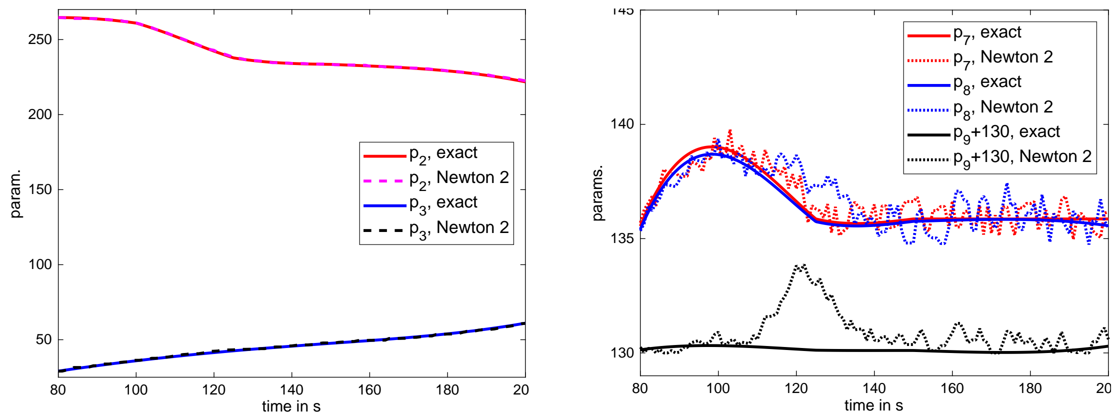

Figure 19: Exact and reconstructed parameters p_2 and p_3 (left) and p_7, p_8, and p_9 (right) for measurement data with $\sigma = 0.1$.

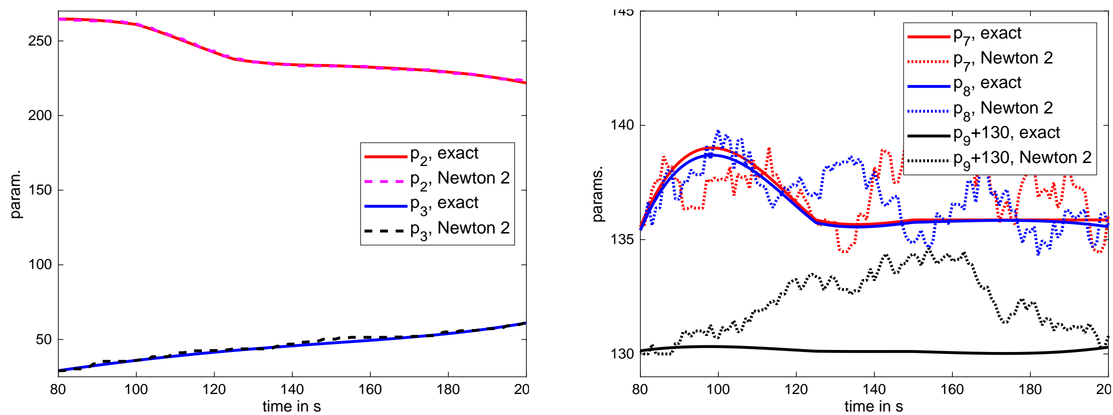

Figure 20: Exact and reconstructed parameters p_2 and p_3 (left) and p_7, p_8, and p_9 (right) for measurement data with $\sigma = 0.5$.

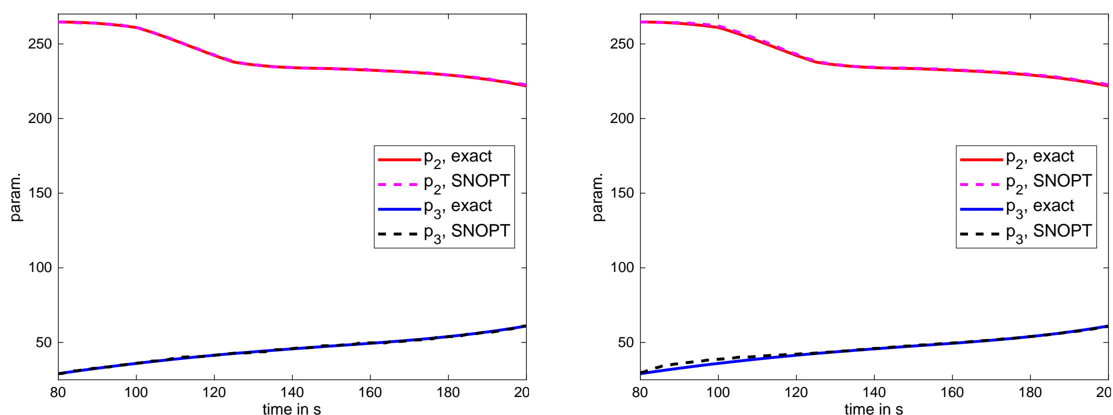

Figure 21: Exact and reconstructed parameters p_2 and p_3 for measurement data with $\sigma = 0.1$ determined together with p_7, p_8, and p_9 (left) and determined with fixed estimated parameters p_7, p_8, and p_9 (right).

DOI 10.20347/WIAS.PREPRINT.2564 Berlin 2018

the etching into the silicon takes 120 seconds. The numerical computation has been performed on a laptop (one processor of Intel i7-4700MQ CPU with 2.40 GHz).

9 Conclusions

The control of etching processes requires a fast in-situ measurement of the geometrical parameters of the developing surface structure. To establish and test such measurement procedures in a realistic situation, a special Reactive-Ion-Etching of a special periodic structure over silicon was fixed (cf. Sect. 2). In order to get a dynamically changing surface geometry, the process was started and interrupted at few different time points less than the full period. The geometry parameters were determined from SEM images and interpolated over the full time period. In a different run of an identical process, the reflectivity spectrum of the geometry was measured by a new device, developed by the LayTec company. This device determines the time-depending reflectances of the evolving surface during the etching at time steps less than a second. The examples of Sect. 4 show a relatively good agreement of the measured spectra with those obtained by numerical simulation. However, probably due to model errors for the geometry, the simulation of the dynamical process was still not sufficiently accurate. To continue the analysis, reflectance spectra including random perturbations of different levels were simulated.

If the reflectance spectrum is given, then a numerical algorithm is needed, which converts the measured data into the geometrical parameters. To employ this in the etching process in short time steps, a fast algorithm is needed. As demonstrated in Sect. 9, this algorithm can be chosen as a classical inverse solver based on nonlinear optimization. However, since such classical methods include lengthy direct computations of the spectrum for given geometry parameters, the computations should be replaced by an interpolation of spectra from a library of precomputed spectra. The presented algorithm uses a library based on sparse grids and on reduced spectra, which are optimized by a sensitivity technique. For the realistic example of an etching process mentioned above, it is shown that, from the mathematical point of view, the essential geometry parameters can be reconstructed fast enough to trace the etching process. However, the geometrical model for the surface and the measured reflectance values must be of high accuracy, otherwise the reconstructed parameters do not follow the exact values of the process. Unfortunately, the geometrical model and/or the measured reflectance spectra were still not sufficiently accurate for the recovery. To exclude these still existing systematic errors, a further thorough analysis of the geometry in the etching process is needed.

References

[1] T. ABBOUD, Formulation variationnelle des équations de Maxwell dans un réseau bipériodique de $\mathbb{R}^3$, *C.R. Acad. Sci. Pairs*, **317**, pp. 245–248, 1993.

[2] R.M. AL-ASSAD AND D.M. BYRNE, Error analysis in inverse scattering. I. Modeling, *J. Opt. Soc. Amer. A*, **24** (2), pp. 326–338, 2007.

[3] H. AMMARI, Uniqueness theorems for an inverse problem in a doubly periodic structure, *Inverse Problems*, **11**, pp. 823–833, 1995.

[4] H. AMMARI AND G. BAO, Coupling of finite element and boundary element methods for the scattering by periodic chiral structures, *Journal of Computational Mathematics*, **3**, pp. 261–283, 2008.

[5] N. ANTTU AND H.Q. XU, Scattering matrix method for optical excitation of surface plasmons in metal films with periodic arrays of subwavelength holes, *Physical review B*, **83**, 165431, pp. 165431-1–165431-17, 2011.

[6] G. BAO, Finite element approximation of time harmonic waves in periodic structures, *SIAM J. Numer. Anal.*, **32**, pp. 1155–1169, 1995.

[7] G. BAO, Variational approximation of Maxwell's equation in biperiodic structures, *SIAM J. Appl. Math.*, **57**, pp. 364–381, 1997.

[8] G. BAO AND D.C. DOBSON, On the scattering by biperiodic structures, *Proc. Am. Math. Soc.*, **128**, pp. 2715–2723, 2000.

[9] M. BÄR, B. BODERMANN, H. GROSS, R. MODEL, M. WURM, AND A. RATHSFELD, Mathematical modelling of indirect measurements in scatterometry, *Measurement*, **39**, pp. 782–794, 2006.

[10] O.P. BRUNO, F. REITICH, Numerical solution of diffraction problems: a method of variation of boundaries. III. Doubly periodic gratings, *J. Opt. Soc. Amer. A*, **10** (12), pp. 2551–2562, 1993.

[11] X. CHEN AND A. FRIEDMAN, Maxwell's equations in a periodic structure, *Transactions AMS*, **323**, pp. 465–507, 1991.

[12] D.C. DOBSON, A variational method for electromagnetic diffraction in biperiodic structures, *RAIRO Model. Math. Anal. Numer.*, **28**, pp. 419–439, 1994.

[13] J. ELSCHNER, R. HINDER, G. SCHMIDT, Finite element solution of conical diffraction problems, *Advances in Comp. Math.*, **16**, pp. 139–156, 2002.

[14] Y. FENG, P. KUMAR, AND A.D. BAILEY, Method of feature exaction from time-series of spectra to control endpoint of process, *United States Patent Application Publication*, US **2018/0182632** A1, 2018.

[15] P.E. GILL, W. MURRAY, AND M.A. SAUNDERS, SNOPT: An SQP algorithm for large-scale constrained optimization, *SIAM Rev.*, **47** (1), pp. 99–131, 2005.

[16] H. GROSS, S. HEIDENREICH, AND M. BÄR, Impact of different stochastic line edge roughness patterns on measurements in scatterometry - a simulation study, *Measurement*, **98**, pp. 339–346, 2017.

[17] H. GROSS, S. HEIDENREICH, M.-A. HENN, M. BÄR, AND A. RATHSFELD, Modeling aspects to improve the solution of the inverse problem in scatterometry, *Discrete and Continuous Dynamical Systems S*, **8** (3), pp. 497–519, 2015.

[18] H. GROSS AND A. RATHSFELD, Sensitivity analysis for indirect measurement in scatterometry and the reconstruction of periodic grating structures, *Waves in Random and Complex Media*, **18**, pp. 129–149, 2008.

[19] G. GRANET AND J. CHANDEZON, The method of curvilinear coordinates applied to the problem of scattering from surface-relief gratings defined by parametric equations: application to scattering from cycloidal grating, *Pure Appl. Opt.*, **6**, pp. 727–740, 1997.

[20] S. HEIDENREICH, H. GROSS, AND M. BÄR, Bayesian approach to the statistical inverse problem of scatterometry: Comparison of three surrogate models. *International Journal for Uncertainty Quantification*, **5** (6), pp. 511–526, 2015.

[21] M.-A. HENN, H. GROSS, S. HEIDENREICH, F. SCHOLZE, C. ELSTER, AND M. BÄR, Improved reconstruction of critical dimensions in extreme ultraviolet scatterometry by modeling systematic errors, *Measurement Science and Technology*, **25** (4), 044003, 2014.

[22] G. HU AND A. RATHSFELD, Convergence analysis of the FEM coupled with Fourier-mode expansion for the electromagnetic scattering by biperiodic structures, *Electronic Transaction on Numerical Analysis.*, **41**, pp. 350–375, 2014.

[23] M. HUBER, J. SCHOEBERL, A. SINWEL, AND S. ZAGLMAYR, Simulation of diffraction in periodic media with a coupled finite element and plane-wave approach, *SIAM J. Sci. Comput.*, **31**, pp. 1500–1517, 2009.

[24] B.H. KLEEMANN, *Elektromagnetische Analyse von Oberflächengittern von IR bis XUV mittels einer parametrisierten Randintegralmethode: Theorie, Vergleich und Anwendungen*, Dissertation, TU Ilmenau, 2002, Mensch & Buch Verlag, Berlin, 2003.

[25] L. LI, Justification of matrix truncation in the modal methods of diffraction gratings, *J. Opt. A: Pure Appl. Opt.*, **1**, pp. 531–536, 1999.

[26] D. MAYSTRE, Integral methods. In: *Electromagnetic theory of gratings*, R. Petit, ed., Springer-Verlag, Berlin, pp. 63–100, 1980.

[27] M.G. MOHARAM AND T.K. GAYLORD, Rigorous coupled wave analysis of planar grating diffraction, *J. Opt. Soc. Amer.* **71**, pp. 811–818, 1981.

[28] M. NEVIÈRE AND E. POPOV, *Light propagation in periodic media*, Marcel Dekker, Inc., New York, Basel, 2003.

[29] J. NOCEDAL AND S.J. WRIGHT, *Numerical Optimization*, Springer Series in Operation Research, Springer, New York, Inc., 1999.

[30] R. PETIT, ed., *Electromagnetic theory of gratings*, Springer-Verlag, Berlin, pp. 63–100, 1980.

[31] A. POMP, The integral method for coated gratings: computational cost, *J. Mod. Optics* **38**, pp. 109–120, 1991.

[32] J. POMPLUN, *Reduced basis method for electromagnetic scattering problems*, Dissertation, FU Berlin, 2009.

[33] E. POPOV, ed., *Gratings: Theory and Numerical Applications*, Presses universitaires de Provence (PUP), www.fresnel.fr/numerical-grating-book-2, 2012.

[34] N. POSSEME, ed., *Plasma etching processes for CMOS device realization*, ISTE-Press Elsevier, 2017.

[35] D.W. PRATHER, M.S. MIROTZNIK, AND J.N. MAIT, Boundary integral methods to the analysis of diffractive optical elements, *J. Opt. Soc. Am. A*, **14**, pp. 34–42, 1997.

[36] G. SCHMIDT, On the diffraction by biperiodic anisotropic structures, *Applicable Analysis*, **82**, pp. 75–92, 2003.

[37] G. SCHMIDT, Electromagnetic scattering by periodic structures, *Journal of Mathematical Sciences*, **124** (6), pp. 5390–5405, 2004.

[38] S.A. SMOLYAK, Quadrature and interpolation formulas for tensor products of certain classes of functions, in Russian, *Dokl. Akad. Nayk SSSR*, **148**, pp. 1042–1045, 1963.

[39] M.D. TETIKER, S. SRIRAMAN, A.D. BAILEY, A. PATERSON, AND R.A. GOTTSCHO, Methods and apparatuses for etch profile optimization by reflectance spectra matching and surface kinetic model optimization, *United States Patent Application Publication*, US **2017/0371991** A1, 2017.

[40] M.D. TETIKER, S. SRIRAMAN, A.D. BAILEY, A. PATERSON, AND R.A. GOTTSCHO, Methods and apparatuses for etch profile optimization by reflectance spectra matching and surface kinetic model optimization, *United States Patent*, US **9 996 647** B2, 2018.

[41] A.V. TISHCHENKO Generalized source method: New possibilities for waveguide and grating problems, *Opt. and Quantum Electron.* **32**, pp. 871–980, 2000.

[42] J. TURUNEN AND F. WYROWSKI, eds., *Diffractive optics for industrial and commercial applications*, Akademie Verlag, Berlin, 2003.

[43] H.P. URBACH, Convergence of the Galerkin method for two-dimensional electromagnetic problems, *SIAM J. Numer. Anal.*, **28**, pp. 697–710, 1991.

[44] V.C. VENUGOPAL, Process endpoint detection metod using broadband reflectometry, *United States Patent*, US **6 979 578** B2, 2005.

[45] Y. WU AND Y.Y. LU, Analyzing diffraction gratings by a boundary integral equation Neumann-to-Dirichlet map method, *J. Opt. Soc. Am. A*, **26** (11), pp. 2444–2451, 2009.